Plate impact experiments to investigate shock-induced inelasticity in Westerly granite

Fuping Yuan [a,b], Vikas Prakash [a,*]

[a] Case School of Engineering, Department of Mechanical and Aerospace Engineering, Case Western Reserve University, Cleveland, OH 44106-7222, USA
[b] State Key Laboratory of Nonlinear Mechanics, Institute of Mechanics, Chinese Academy of Sciences, Beijing 100190, China

ARTICLE INFO

ABSTRACT

In the present study, plate-impact experiments are employed to better understand the stress threshold for inelasticity in Westerly granite. The experiments are designed to obtain the Hugoniot Elastic Limit (HEL) as well as spall strength following shock-induced compression in the Westerly granite samples. The HEL for Westerly granite is estimated to be in the range 3.2 to 3.5 GPa, while the spall strength is ~50 MPa for a pulse duration of 3 µs, and is nearly independent of the compression stress level in the stress range employed in the experiments (i.e. 0.7–5.0 GPa). In addition, soft-recovery plate-impact experiments are employed to better understand the threshold for initiation of micro-cracking in the granite samples. These recovery experiments are conducted at the same stress levels as the normal plate impact experiments (~0.7 GPa), and the duration of the tensile pulse is varied from 20 to 500 ns by varying the pre-set gap between the specimen and the momentum trap. The results indicate that the stress pulse duration threshold for initiation of spall is about 120 ns at an applied tensile stress level of ~0.7 GPa. In addition, tensile fracture in Westerly granite is observed to be time dependent with the spall strength dependent on the duration of the tensile pulse. For the soft recovery experiments that do not show a clear spall signal, the recovered granite specimens show relatively large micro-cracks (30–40 µm in width) near the plane where the unloading waves from the flyer and target free surfaces intersect. The spall plane reveals a relatively rough and a tortuous fracture surface. At higher magnifications, several cracks and pits/holes are detected on the spall plane. The fracture/damage mode is seen to be predominantly brittle, with damage initiating at the weak grain boundaries.

1. Introduction

Shock-induced response of geological materials has been the focus of attention for last several decades due to its applications in planetary impact, explosive crater formations, response of geo-materials to blast/explosive loading, rock fragmentation research [1–9], to name a few. In these applications strain rates of the order of 10^5 s^{-1} and higher are common and the loading process is usually adiabatic. In order to better understand the various deformation mechanisms and failure, it is important to characterize shock response in geological materials under well-characterized loading conditions.

Shock-induced properties of geological materials have been investigated using a variety of techniques including explosive detonation loading, impact cratering experiments, and flyer-plate impact studies. For example, Kovalev et al. [10] used explosive

loading along with manganin pressure gages to investigate elasto-plastic shock-wave profiles in marble, quartzite and granite. They found the shock-wave front to split into a leading elastic pre-cursor followed by a plastic (in-elastic) compressive wave; the amplitude of the elastic precursor is observed to decrease with increasing propagation distance in the samples. Tilert et al. [9] studied explosively-induced movement as well as spall due to buried detonation charges in granite blocks with thicknesses in the range 60–300 mm. Their results suggest a critical spall distance of around 210 mm for buried charges of 1 g high explosives, beyond which no spalling was observed. Ai and Ahrens [6] measured compressional wave speeds as well as attenuation coefficients in 1 cm cube samples cut from a San Marcos granite block recovered from a lead bullet impact cratering experiment. Based on the measured longitudinal wave (P-wave) velocities in three orthogonal directions, they obtained an estimate for the damage parameters in the shocked granite.

In order to further investigate the shock behavior in geological materials, e.g. the shock Hugoniot curve, Hugoniot elastic limit (HEL), dynamic shear strength, and spall strength under well controlled shock wave loading conditions, normal plate-impact experiments

have been routinely utilized along with state-of-the-art techniques for stress and/or particle velocity measurements. For example, Grady and Hollenbach [11] used an optical interferometer to measure the free-surface pull-back signal and found that the dynamic tensile fracture strength of a crustal rock is rate-dependent in the range of a few tens of MPa to 100 MPa. Cohn and Ahrens [12] conducted a microscopic examination of polished thin sections of recovered post-test rock samples following shock loading to determine their incipient spall strength. In their analysis they assumed the stress above which microscopically observable cracks appear in the samples to correspond to the dynamic tensile strength. Ahrens and Rubin [2] used ultrasonic measurements on post-test plate-impact specimens of Bedford limestone to relate shock-induced damage to tensile stresses. Millett and Tsembelis [3] employed embedded manganin stress gages to measure both longitudinal and lateral stresses in two different igneous rocks to estimate their shear strength under shock wave loading. Willmott and Proud [8] used embedded manganin gages as well as laser-based diagnostics to determine the shock Hugoniot curve of a Kimberlite (Tuffisitic Kimberlite Breccia, TKB) between 0.3 and 8.4 GPa. In their work, inelastic deformation was observed at all stresses due to a combination of volume compaction and brittle failure. Also, their results suggested a HEL between 0.6 and 0.9 GPa for TKB.

The results obtained from the above mentioned shock wave studies have been problematic. For example, micro-cracking inferred from the microscopic examination of post-shocked specimens depends critically on the position (plane) where the sample is sectioned. In addition, the sample-cutting process have been known to introduce artificial damage. The ultrasonic measurements were based on volume measurements, which can provide excellent estimates of the density of micro-cracks but does not provide quantitative information on the shock-induced properties of geological materials. Also, while embedded manganin stress gages can provide stress in the sample directly, the gage itself can affect stress wave propagation in the samples. In addition, shock-induced properties of geological materials, such as the HEL and spall strength, are highly dependent on the strain rate, as well as the amplitude and duration of the incident stress pulse. As a result, accurate measurements and quantitative data on the shocked-induced properties of rocks and their dependence on strain rate and characteristics (amplitude and duration) of the stress wave are still lacking.

In the present study, we seek to study these issues by conducting novel plate impact experiments designed specifically to investigate inelasticity and shock-induced response in Westerly granite rock samples. A multi-beam VALYN VISAR™ (Velocity Interferometer for Any Reflector) is employed [13] to measure the free surface particle velocity, which is also used to calculate the stress state in the samples. Using these experimental techniques, the HEL as well as spall strength following shock-induced compression in Westerly granite samples are obtained. In addition, soft recovery plate-impact experiments are conducted to understand the threshold for the initiation of micro-cracking in Westerly granite. This is achieved by proper choice of flyer geometry (star-shaped) and a momentum trap placed behind the target specimen. The momentum trap prevents reloading of the specimen except of an initial tensile pulse reflected from a pre-set gap between the specimen and the momentum trap. Moreover, detailed microstructural analyses of the post-test recovered specimen are conducted to better understand the relationship between the extent of damage and the tensile stress pulse duration.

1.1. Plate impact spall experiments

In the present stduy normal plate-impact experiments are conducted to investigate spall strength in Westerly granite using

a 82.5 mm bore single-stage gas-gun facility at Case Western Reserve University. Fig. 1 shows the schematic of the plate-impact experimental configuration. A fiberglass projectile carrying a flyer plate is accelerated down the gun barrel by means of compressed nitrogen. The rear end of the projectile has sealing O-ring and a Teflon key that slides in a key-way inside the gun barrel to prevent any rotation of the projectile. In order to load the granite specimens in shock-compression a metal flyer is impacted with the thick granite target plate. A polymethyl methacrylate (PMMA) window plate, with a thin aluminum coating ($\sim$100 nm), is placed behind the granite target plate to provide a reflective surface to enable particle velocity measurements by using a laser interferometer. In order to reduce the possibility of an air cushion between the flyer and target plates, the target chamber is evacuated to 50 μm of Hg prior to impact. A laser-based optical system utilizing a Helium–Neon 5 mW laser and a high frequency photo-diode is used to measure the velocity of the projectile. To ensure generation of plane-waves with wave front sufficiently parallel to the impact face, the flyer and the target plates are carefully aligned to be parallel to within 2×10^{-5} rad by using an
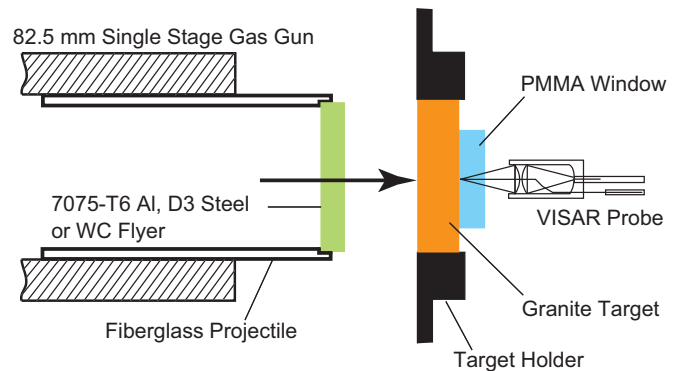

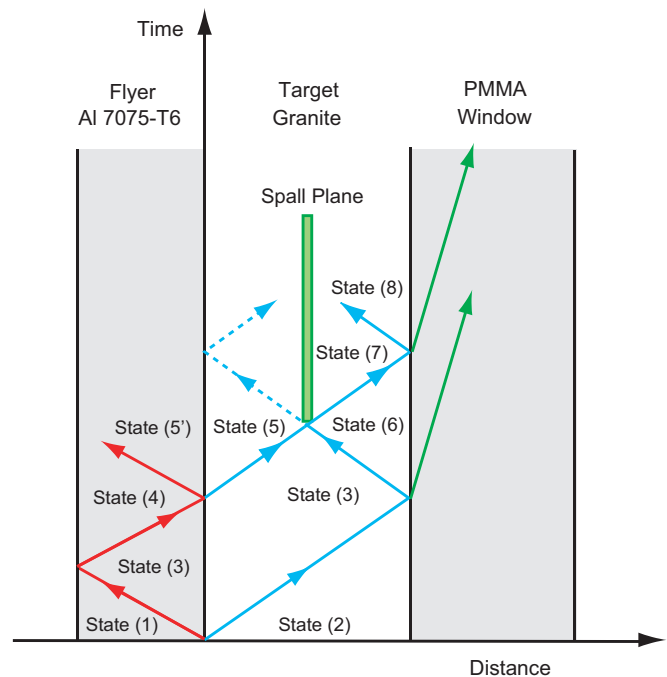
Fig. 1. Schematic of the plate-impact spall experiment.

Fig. 2. Wave Propagation in the flyer and the target plates (*t*–*X* diagram) for a typical plate-impact spall experiment.
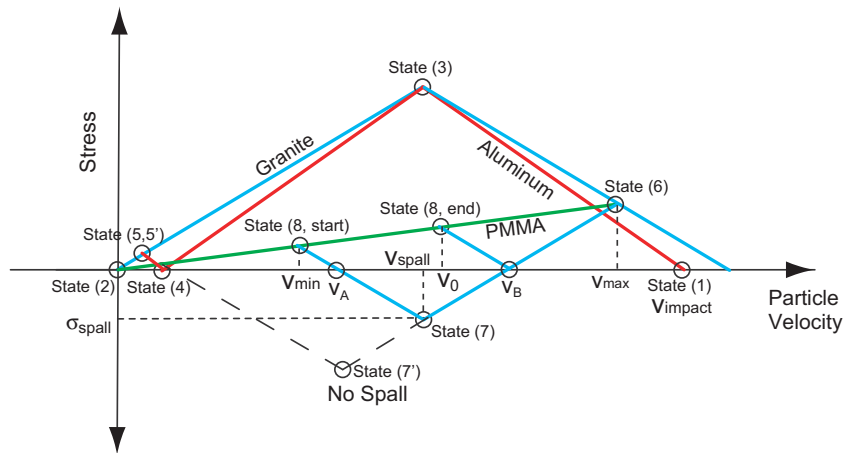
Fig. 3. Normal-stress versus particle-velocity (S–V) diagram for a typical plate-impact spall experiment.

optical alignment scheme developed by [14]. The actual tilt between the two plates is measured by recording the times at which four, isolated, voltage-biased pins, that are flush with the surface of the target plate, are shorted to ground. A velocity interferometer is used to measure the history of the normal particle velocity at interface between the granite plate and PMMA window. The multi-beam VALYN VISAR™ is used as the interferometer system to measure the free surface particle velocity history at the rear surface of the target plate. A 5 W solid-state diode-pumped frequency doubled Nd:YVO$_4$ CW laser with wavelength of 532 nm is used to provide a coherent monochromatic light source. All measurements of the particle velocity are made before the arrival of the release waves from the lateral boundary of the specimen. In view of this, and during the time interval of interest, the flyer and target plates can be considered to be essentially infinite in their spatial dimensions and one-dimensional wave theory is used in the interpretation of the experimental results. Other details regarding the experimental configuration and execution of the experiments can be found elsewhere [15–17].

The schematic of the t–X (time vs. distance) diagram, which illustrates the propagation of compression and tensile waves through the target and flyer plates during a typical plate-impact spall experiment, is shown in Fig. 2. The abscissa represents the distance in the target and the flyer plates from the impact surface, while the ordinate represents the time after impact. The arrows indicate the direction of wave propagation. Upon impact, longitudinal compressive waves are generated in both the target and the flyer plates, resulting in compression loading in the granite target. The interaction of the corresponding release longitudinal waves from the free surface of flyer and interface between the target plate and PMMA window brings the shocked material into a state of tensile stress at a pre-determined location within the granite specimen. If the tensile stress exceeds a critical strength value for the material (spall strength), a tensile damage process is initiated and eventually spall (material separation) occurs if both the amplitude and the pulse duration of the tensile wave are sufficient. The occurrence of spall can be inferred from the measured free-surface particle velocity versus time profiles.

The S–V (stress vs. particle velocity) diagram details the locus of all the normal stress and particle-velocity states that can be attained during a typical plate-impact spall experiment. Fig. 3 illustrates the normal stress and particle velocity in the various shock states. The abscissa represents the particle velocity in the target and the flyer plates while the ordinate represents the normal stress in the target and flyer. For the case in which the spall strength is greater than the applied tensile stress, the normal
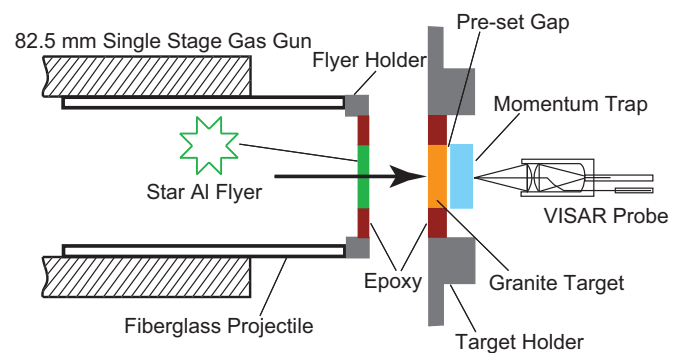

Fig. 4. Schematic of the soft-recovery plate-impact experiment.

stress and particle velocity states in the granite moves along the dashed lines from State 5 to the no-spall-state, denoted by State (7'). However, if the tensile stress is greater than the spall strength of the granite (σ_{spall} indicated by the short dashed lines), the granite will spall and the tensile stress in State (7) will unload to the stress state denoted by State (8). The compressive "end of spall" wave arrives at the interface between the granite target plate and PMMA window, and brings the free surface velocity to State (6). The free surface particle velocity in States 6 is referred to as V_{max}, and the corresponding free surface particle velocity in State 8 is denoted by V_{min}. The spall strength, σ_{spall}, can then be calculated from the measured particle velocities V_{max} and V_{min}, by using:

$$\sigma_{spall} = \frac{(V_B - V_A)}{2}(\rho C_L)_{granite} \tag{1}$$

where

$$V_B = \frac{(\rho C_L)_{granite} - (\rho C_L)_{PMMA}}{(\rho C_L)_{granite}} V_{max}, \text{ and}$$

$$V_A = \frac{(\rho C_L)_{granite} + (\rho C_L)_{PMMA}}{(\rho C_L)_{granite}} V_{min}$$

In Eq. (1), $(\rho C_L)_{granite}$ and $(\rho C_L)_{PMMA}$ represent the longitudinal impedance of granite and PMMA respectively.

1.2. Soft recovery plate impact experiments

Fig. 4 shows the schematic of the soft recovery plate impact experiments. The soft recovery of the impacted specimen is achieved by proper choice of flyer geometry and loading
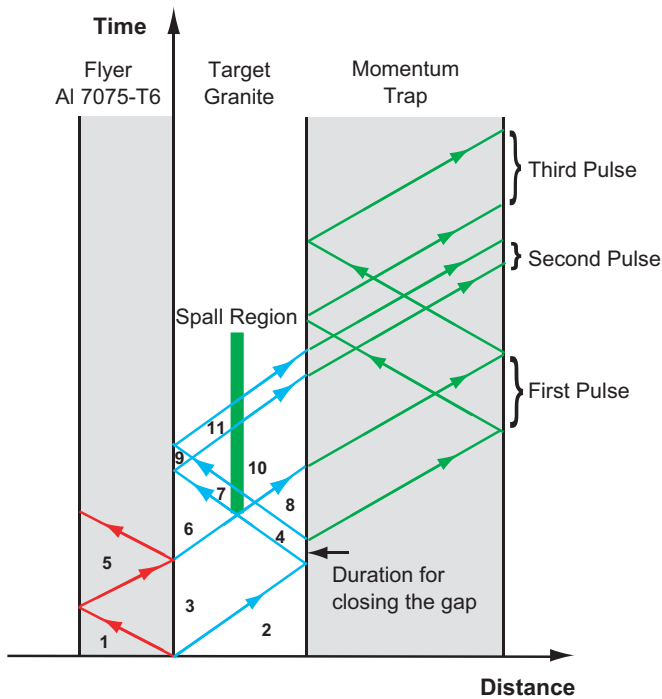
Fig. 5. Wave Propagation in the flyer and the target plates (*t–X* diagram) for a typical soft recovery plate-impact experiment.
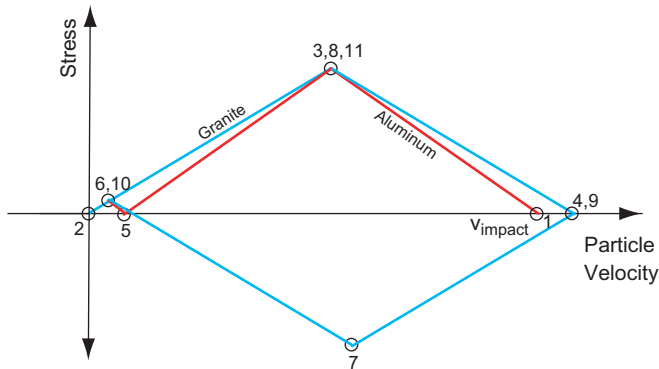

Fig. 6. Normal-stress versus particle-velocity (*S–V*) diagram for a typical soft recovery plate-impact experiment.

conditions such that damage is confined to regions of highly localized stresses and the surrounding regions of lower stress provide resistance to the coalescence and propagation of macro-cracks. In order to achieve this, an eight-pointed star-shaped flyer [18,19] is used to subject a central octagonal region of the granite specimen to a plane compressive pulse. A momentum trap (quartz) sitting behind the target specimen is used to prevent reloading of the specimen except of an initial tensile pulse reflected from a pre-set gap between the specimen and the momentum trap. In order to initiate various levels of micro-structural damage in the granite specimen, the duration of the tensile pulse is varied by the magnitude of the gap. In particular, the results of the experiments help us to establish a threshold for tensile pulse duration for the occurrence of spall.

In order to understand the loading history in the central region of the granite specimen we consider a linear elastic wave analysis of the impact problem. Figs. 5 and 6 show the *t–X* (time vs. distance) diagram and the S–V (stress vs. particle velocity) diagram for the soft recovery experiments. Upon impact, two

compression waves are generated from the impact surface. One wave travels into the star flyer, and the other travels into granite causing the compressive stress. When the first part of the compressive pulse reaches the rear surface of the granite specimens, the gap between and the granite specimen and the momentum trap causes the surface of the granite specimen to act like a free surface for a time equal to the time for the particle velocity to close the gap. Before the gap is closed, the interaction of the corresponding release (unloading longitudinal wave) from the free surfaces of flyer and the target plates brings the shocked granite material to a state of tensile stress (State 7). Next, the tensile wave reflects at the interface between the star flyer and the granite specimen as a compressive pulse, which travels through the specimen (State 11) before entering the momentum trap. The initial compressive pulse (minus the reflected part at the target/momentum–trap interface) travels through the momentum trap, reflects from the free surface, and becomes a tensile pulse. When this tensile pulse reaches the interface between the granite specimen and the momentum trap, the momentum trap separates from the granite specimen, since this interface cannot support tension. The momentum trap flies off, leaving the specimen nearly unstressed and with essentially zero momentum. The specimen can then be recovered and examined in more detail to determine the type and extent of damage from the loading history.

2. Experimental results

2.1. Plate-impact spall experiments

In the present study, a total of seven normal plate-impact experiments were conducted on Westerly granite to obtain its HEL and spall strength. Five of these experiments were conducted with an aluminum flyer plate, one with a steel flyer, and one with a tungsten carbide (WC) flyer. Table 1 lists the key parameters for the seven experiments—it provides the Shot #, thickness of the granite target plate, thickness of the flyer plates, impact velocity, and the shock-induced compressive stress level at impact. Table 2

Table 1
Summary of the plate-impact experiments on Westerly granite.

Exp. no.	Flyer (mm)	Target granite (mm)	Impact velocity (m/s)	Impact stress (GPa)
Shot 6	Al, 8.85	19.05	91.5	0.7
Shot 4	Al, 9.12	18.90	156.5	1.2
Shot 3	Al, 8.95	18.70	249.1	1.8
Shot 1	Al, 8.95	19.01	364.5	2.9
Shot 2	Al, 8.93	19.27	561.3	3.9
Shot 5	Steel, 8.55	19.20	491.5	5.0
Shot 7	WC, 6.00	19.01	489.4	5.8

Table 2
Material density, longitudinal wave speed, and the elastic longitudinal impedance, for the Westerly granite specimen, aluminum flyer plate, steel flyer plate, and the WC flyer plate, used in the present study.

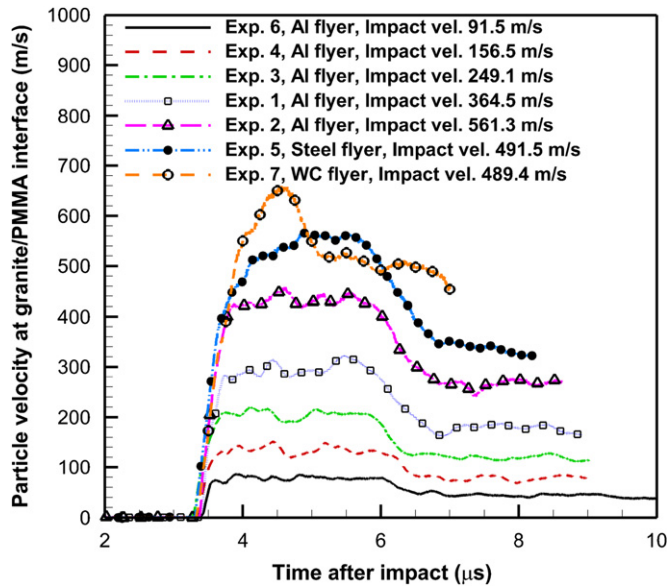|	Density g/cm³	Longitudinal wave speed km/s	Longitudinal impedance GPa/(mm/µs)
Westerly granite specimen	2.6	5.4	14.04
Aluminum flyer plate	2.8	6.23	17.44
Steel flyer plate	7.86	5.98	47.00
WC flyer plate	15.2	6.99	106.25

Fig. 7. Particle-velocity versus time profiles for seven normal plate-impact experiments conducted in the present study.
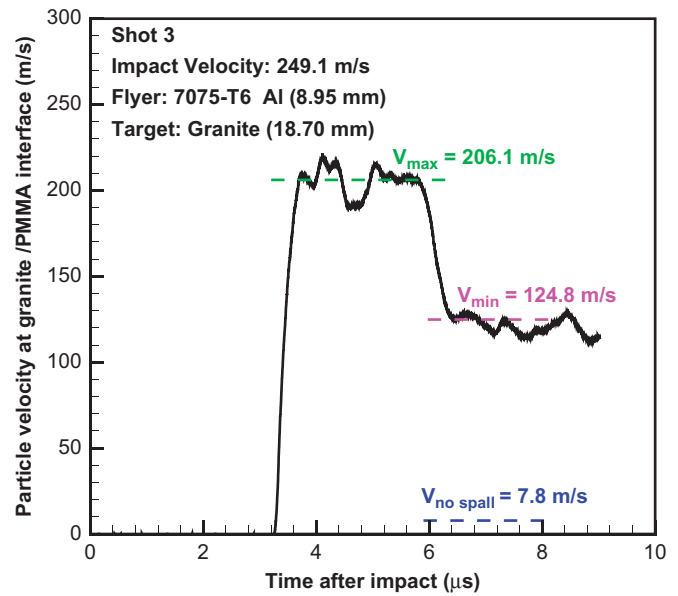

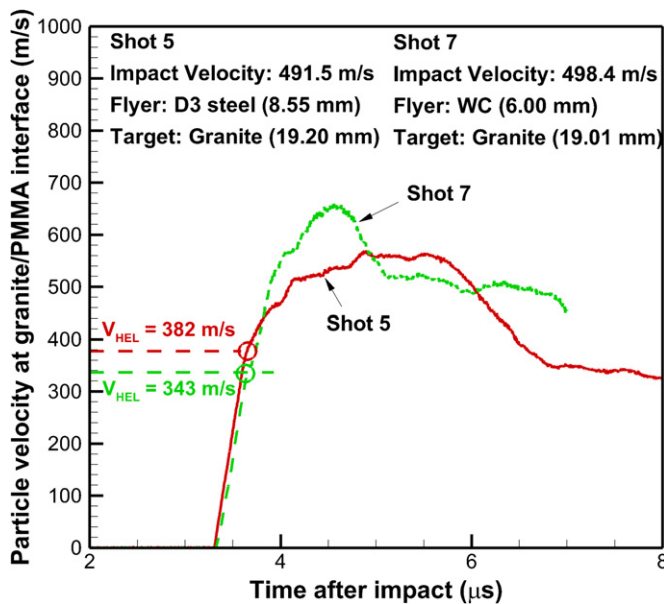Fig. 9. Calculation of spall strength illustrated for Shot 3.

Fig. 8. Calculation of Hugoniot Elastic Limit (HEL) for Westerly granite from the measured particle velocity profiles.

Fig. 10. Spall strength vs. impact stress for Westerly granite.

lists the density, the longitudinal wave speed and the longitudinal impedance of all the plates and the specimen used in the experiments. The shock-induced impact stresses were estimated from the measured impact velocity and the knowledge of the elastic longitudinal impedance of the Westerly granite target and the flyer plates.

Fig. 7 shows the measured particle-velocity profiles for all the seven experiments. At higher impact stresses (Shots 5 and 7), the measured particle-velocity profiles (shown in Fig. 8) show a clear two-wave structure indicative of elastic-plastic response. The kink in the two-wave structure is used to estimate the HEL for the Westerly granite specimens. From the profiles shown in Fig. 8, the particle velocities at the HEL for Westerly granite V_{HEL}, are measured to be 343 m/s and 382 m/s for Shots 5 and 7, respectively. From these particle velocity measurements the HEL can be
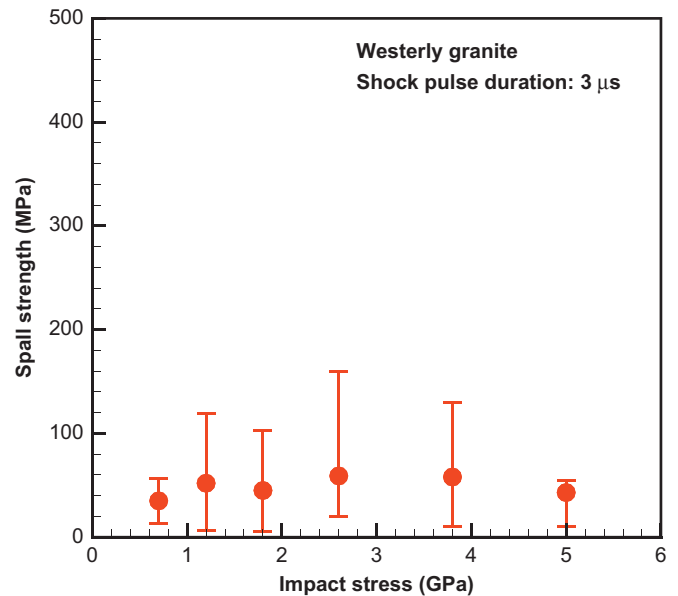
estimated by using:

$$\sigma_{HEL} = \frac{(\rho C_L)_{granite} + (\rho C_L)_{PMMA}}{2(\rho C_L)_{granite}} (\rho C_L)_{granite} V_{HEL}, \quad (2)$$

where, $(\rho C_L)_{granite}$ and $(\rho C_L)_{PMMA}$ are the longitudinal impedances for granite and PMMA, respectively. From these measurements the spall strength in Westerly granite is estimated to be in the range of 3.2 to 3.5 GPa.

Fig. 9 shows typical particle velocity data for Shot 3 that is used to estimate the spall strength of the Westerly granite rock sample. At the arrival of the compression wave at the free surface of the target plate, the particle velocity increases to V_{max}. Due to the inherent heterogeneity of the Westerly granite rock samples, the measured particle velocity profiles are oscillatory in nature and V_{max} is taken to be the average particle velocity during the first shock-induced Hugoniot state. After the spall event,
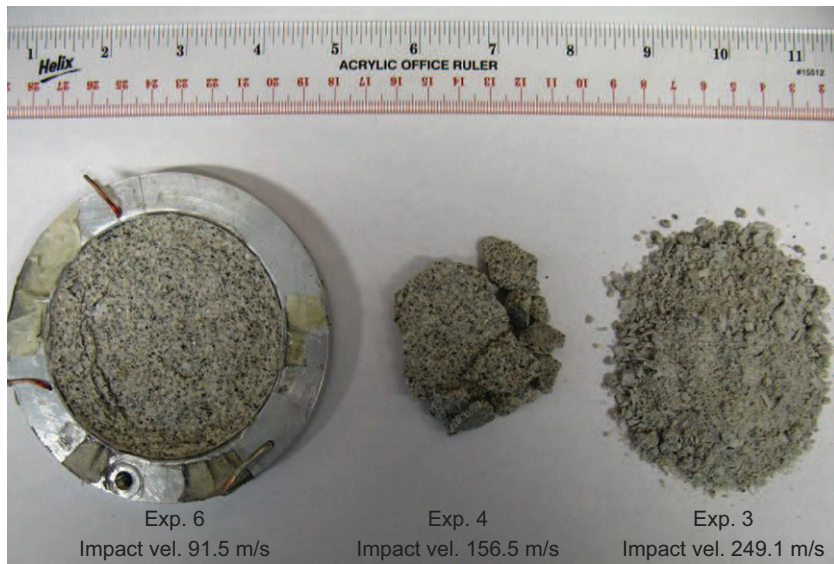
Fig. 11. Post-test specimens for the three normal plate-impact spall experiments.

the particle velocity drops to V_{min}, followed by a pull-back in the particle velocity to V_o. In the spall experiments without the PMMA window plate, V_o is expected to be equal to V_{max}; however, because of the lower impedance of the PMMA window, V_o is observed to be smaller than V_{max}. For the case in which there is no spall, the free-surface particle velocity remains at the state level of $V_{no\text{-}spall}$. Thus, the spall strength of the Westerly granite samples can be estimated by using the pull-back signal and Eq. (2). In this way, for Shot 3, the spall strength of Westerly granite following the shock-induced compression of amplitude 1.8 GPa and a compressive pulse duration of ca. 3 µs is estimated to be 45 MPa.

Fig. 10 shows the spall strength data collected from the five normal plate-impact spall experiments conducted in the present study. Four of these experiments were conducted with an Al alloy flyer plate and one with a steel flyer. The relatively large error bars in the data are due to the stochastic nature of spall in the relatively heterogeneous Westerly granite samples. From these results, the spall strength of the Westerly granite specimens, following shock-induced compression in the range of 0.7–5.0 GPa and with a pulse duration of 3 µs, is found to be only ∼50 MPa and is nearly independent of the applied compression stress levels used in the experiments.

Fig. 11 shows pictures of the post-test impact specimens for Shots 6, 4, and 3. The experiments were conducted with an Al alloy flyer plate at impact speeds of 91.5, 156.5 and 249.1 m/s, respectively. The corresponding impact stresses were 0.7, 1.2 and 1.8 GPa, respectively. At a shock compression level of 0.7 GPa, the post-impact samples show a well-defined spall plane with no apparent fragmentation in the bulk specimen. At higher impact stresses, fragmentation is observed up to a stress level of 1.2 GPa, and at impact stresses above 1.8 GPa the post-test rock samples are essentially reduced to a powder.

2.2. Soft-recovery plate-impact experiments

In the present study six soft-recovery plate-impact experiments are conducted at nearly the same impact stress levels (of about 0.7 GPa), while the duration of the tensile pulse was varied from 20 to 500 ns by changing the pre-set gap between the specimen and the momentum trap. Table 3 provides the details of these six soft-recovery plate-impact experiments. In all tests the thickness of the momentum trap (quartz glass) plate was kept

Table 3
Summary of the soft-recovery plate-impact experiments on the Westerly granite.

Exp. no.	Flyer 7075-T6 (mm)	Target granite (mm)	Impact Velocity (m/s)	Pre-set gap (µm)	Duration of tensile pulse (ns)
Rec03	2.85	5.25	72.9	2	20
Rec02	2.85	5.25	71.3	5	50
Rec01	2.85	5.35	83.9	5	50
Rec06	2.85	5.16	90.8	12	120
Rec05	2.85	5.41	92.1	25	250
Rec04	2.95	5.43	84.8	50	500

Table 4
Material density, longitudinal wave speed, and longitudinal impedance for all plates used in the soft recovery plate impact experiments.

	Density g/cm^3	Longitudinal wave speed km/s	Longitudinal impedance GPa/(mm/µs)
Westerly granite specimen	2.6	5.4	14.04
Aluminum flyer plate	2.8	6.23	17.44
Quartz momentum trap	2.65	5.66	14.99

fixed at 6.65 mm. Table 4 provides the density, longitudinal wave speeds, and longitudinal impedance for all plates used in the soft recovery experiments.

Fig. 12 shows the free-surface particle velocity versus time profile for experiment Rec01. In figure the dashed line represents the elastic prediction (i.e., the expected free surface velocity profile) for no spall. The amplitude of the first compressive pulse is slightly less than predicted by elastic wave theory and decreases slowly with time, indicating the initiation and growth of inelasticity in the granite specimen during dynamic compression. It is interesting to note that there is no pull-back signal at the end of the first compressive pulse, indicating that the 50 ns duration tensile pulse is not sufficient to create spall at a stress level of 0.7 GPa. Moreover, a tail at the end of the compressive pulse is clearly visible. The existence of the tail is a consequence of the accumulation of micro-cracking related damage by the tensile pulse in the rock specimen. The second compression pulse,
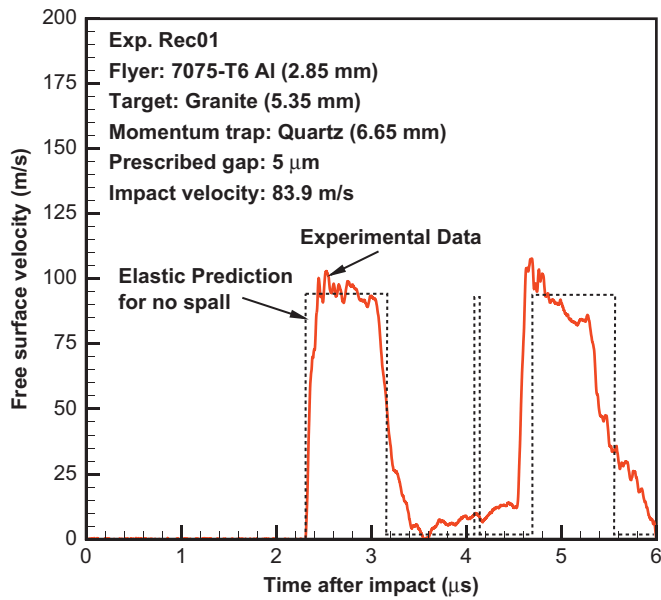
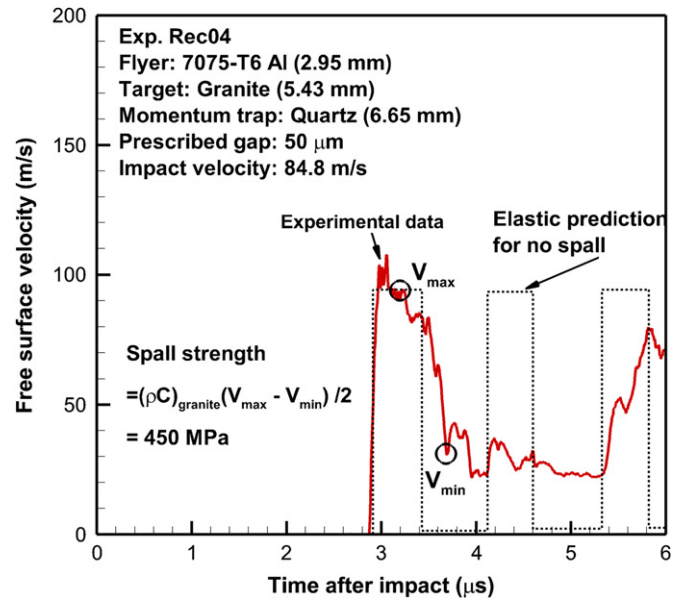**Fig. 12.** Free-surface particle-velocity profile for experiment Rec01.

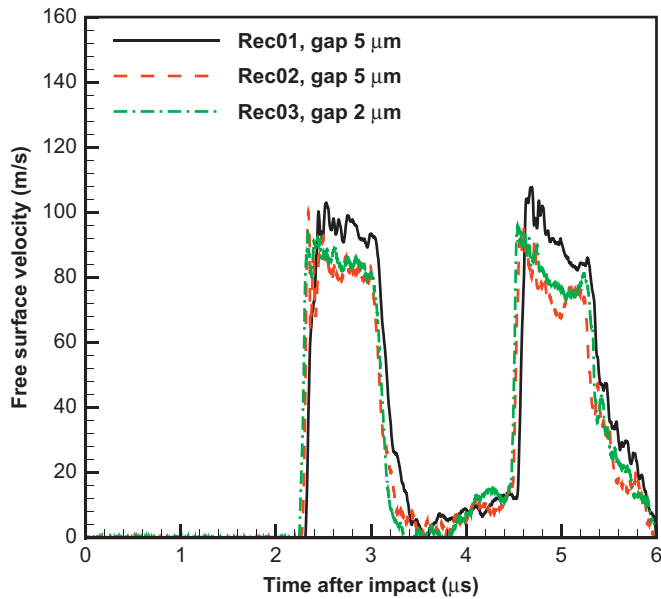**Fig. 14.** Free surface versus particle velocity profile for experiment Rec04.

Fig. 13. Free surface particle velocity profile for experiments Rec03, Rec02 and Rec01.

which was expected to arrive at the monitoring point on the free surface of the target plate at around 4 μs, is not present in the velocity versus time profile. This attenuation of the compression pulse can be attributed to dispersion of the relatively short duration tensile pulse (~50 ns) due to the inherent heterogeneity of the rock microstructure, and also to the accumulation of damage that occurs while the pulse is tensile (i.e., Region 7 in Fig. 5). The amplitude and duration of the second pulse can also be affected by scattering as the reflected compressive pulse travels through the damaged material (i.e., Region 7 in Fig. 5). The other wave signatures, i.e., between the first and the second and the second and third compressive pulses, can be attributed in part to wave spreading during damage in compression and from the simultaneous arrival of the diffracted spherical waves emanating from the re-entrant corners of the star-shaped flyer. The third pulse in Fig. 12 is a reflection of the main compressive pulse after it makes a round trip through the thickness of the

momentum trap. Similarity of the first and the third pulses is an indication of the nearly elastic response of the momentum trap and the dominance of the plane waves in the central region of the specimen. Any inelasticity and/or non-planar wave effects cause the shape and duration of the third pulse to differ from the first. The observed difference in the shape of the first and the third wave profiles is understood to be due to scattering by the heterogeneity in the rock samples and also non-planarity due to the gap between the momentum trap and the granite specimen.

Fig. 13 shows the free surface velocity profile for experiments Rec03, Rec02 and Rec01. The duration of the tensile pulse in these three experiments is varied from 20 to 50 ns. In each case the observed free surface particle velocity is similar to that observed for Shot Rec01—there is an absence of the spall signal following the first compressive wave, and the second compressive wave, which was to arrive at ~4 μs, is absent. Furthermore, the duration of the tail at the end of the first compressive pulse is observed to become longer as the impact velocity is increased. Since the existence of the tail and spreading of the second pulse are immediate consequences of damage due to the tensile pulse, the wave profiles in Fig. 13 indicate that more damage occurs in Shot Rec01 when compared to the other two experiments. The post-test specimens are observed to be radially cracked in each case, perhaps due to a combination of boundary release waves and tensile stresses resulting from bending/flexure of the specimen during impact [18,20]. More importantly, the recovered granite specimens have the same thickness as prior to impact, indicating the absence of spall failure in the three experiments. This is also consistent with the absence of the pull-back signal in the three experiments, indicating that the tensile pulse duration threshold required for spall in Westerly granite is larger than 50 ns at a stress level of 0.7 GPa.

Fig. 14 shows the free-surface particle velocity profile for the experiment Rec04. Unlike Shots Rec01, Rec02 and Rec03, which were conducted with pre-set gaps of 5, 5, and 2 μm, respectively, Shot Rec04 has a pre-set gap of 50 μm, which corresponds to a tensile pulse of duration 500 ns. The dashed line shows the elastic prediction for the case of no spall. The attenuation of the first compressive pulse as a function of time indicates that damage in compression due to micro-cracking occurs in the Westerly granite samples during the passage of the compressive pulse. The pull-back signal corresponding to a spall can be clearly seen at the end
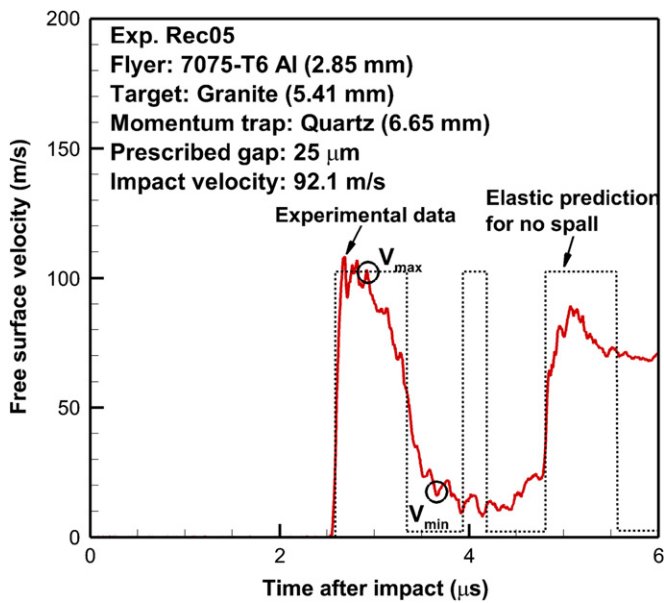
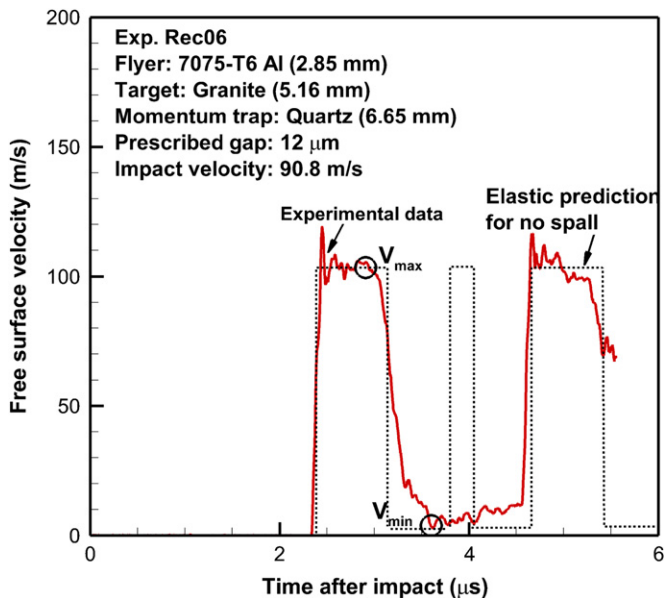**Fig. 15.** Free surface particle velocity versus time profile for experiment Rec05.

Fig. 16. Free surface particle velocity versus time profile for experiment Rec06.

tensile pulse in the Westerly granite samples. Moreover, for experiments Shot Rec05 and Shot Reco 06, a rather large pulse-shape difference is observed between the first and the third compressive waves, indicating that non-planar conditions may be present during the experiment. These non-planar conditions may perhaps be attributed to pre-set gap between the momentum trap and the specimen, which may not be perfectly planar. From experience, it has been difficult to control the planarity of pre-set gaps when rather large gaps are used in plate impact soft recovery experiments.

Optical microscopy examination of the post-test specimens from experiments Rec04, Rec05 and Rec06 indicate a smaller thickness of the recovered specimens when compared to the initial sample thickness, indicating the occurrence of spall during the experiments. Moreover, the average size of the radially fractured pieces is smaller for the case of experiments conducted with a large pre-set gap between the momentum trap and the granite specimen. Again this can be attributed to the combined effects of the longer duration tensile pulse due to the larger pre-set gap between the specimen and the momentum trap and the development of bending stresses in the specimen during impact of the granite target plate with a smaller star-shape flyer.

2.3. Scanning electron microscopy

Soft recovery experiments in which a spall signal was not apparent in the particle velocity versus time profiles (Rec02 and Rec03) but underwent extensive radial macro-cracking, a low magnification optical microscope examination of the impact face yields the presence of a high density of micro-cracks and a few macro-cracks outside the central impact region. This damage pattern is consistent with the tensile stresses induced by the unloading (lateral) cylindrical and spherical waves. At the rear face of the specimen, a damage ring coincident with the eight entrant corners of the flyer plate is also observed. The divergent character of the unloading waves from the corners makes these locations the most favorable regions for stress-induced micro-cracking; consequently, the level of tensile stresses that propagates into the central octagonal region is attenuated to a level below the fracture stress threshold for micro cracking in Westerly granite. The net effect is the generation of a protective ring that eliminates the undesired effects during the generation of the main compressive pulse.

The recovered post-test granite pieces were impregnated in epoxy and then sectioned with a low-speed diamond saw to reveal a surface parallel to the impact direction. Fig. 17 shows the scanning electron microscopy map of a cross-sectional surface parallel to the impact direction for shot Rec02 with the tensile pulse duration of 50 ns. From the figure, it can be seen that even though the specimen did not undergo spall failure, a relatively large micro-crack (about 40 μm in width) is nucleated at the intersection of the two unloading waves from the flyer and target boundaries. The micro-cracking is predominantly inter-granular and is observed to nucleate preferably at the grain boundary between the two grains. Besides this crack, several other smaller micro-cracks are observed on the specimen surface.

Fig. 18 shows the scanning electron microscopy map of the cross-sectional surface parallel to the impact direction for Shot Rec03 (subjected to a tensile pulse of duration of 20 ns). Again, a relatively large micro-crack can be observed in the specimen at the plane where the unloading waves from the flyer and the target intersect. The width of this micro-crack is about 30 μm, which is a little smaller than that observed for shot Rec02, perhaps due to the shorter duration of the tensile pulse. For the soft recovery experiments which indicate a pull-back signal in the particle velocity profile (Rec04, Rec05 and Rec06), a clear spall
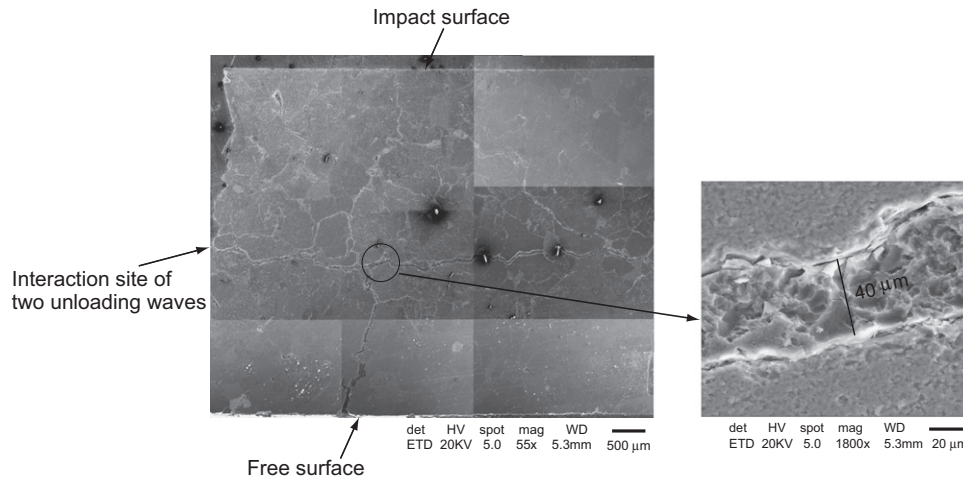
of the first compressive pulse in Fig. 14. The spall strength based on this pull back signal is estimated to be 450 MPa. Fig. 15 shows the particle velocity profile for experiment Rec05, which was conducted with a pre-set gap of 25 μm (which corresponds to tensile pulse duration of 250 ns). Again damage in compression as well as a pull-back signal corresponding to a spall can be seen in the velocity time profile just after the end of the compressive wave pulse. The spall strength was estimated to be 610 MPa. Fig. 16 shows the free-surface particle velocity profile for the experiment Rec06. In this case the pre-set gap is 12 μm, which corresponds to tensile pulse duration of ca. 120 ns. Spall strength of ca. 710 MPa is estimated in this case. In the three experiments, the arrival of the second compressive pulse can be inferred from the measured velocity time profiles; however, the tensile pulse is diffused and has much lower amplitude than that predicted using the elastic wave theory. Again, the strong attenuation of the second compressive pulse can be attributed primarily to the intense damage created by the first compressive pulse and the

Fig. 17. Scanning electron microscopy map of a cross-sectional surface parallel to the impact direction for Shot Rec02 (tensile pulse duration is 50 ns).
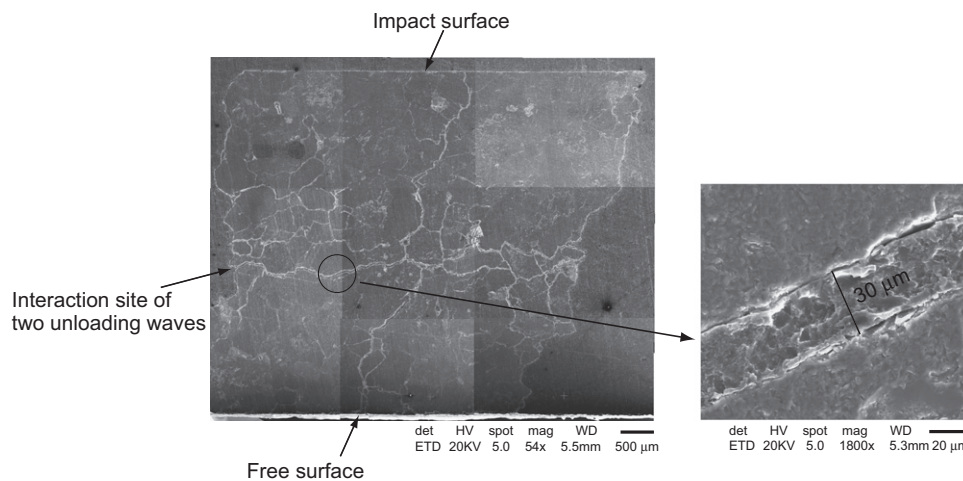

Fig. 18. Scanning electron microscopy map of a cross-sectional surface parallel to the impact direction for Shot Rec03 (tensile pulse duration of 20 ns).

plane can be observed in the post-impacted specimens. The thickness of the post-impacted specimens is observed to be less than the thickness of the specimens prior to the test, further indicating the occurrence of spall in these experiments.

Fig. 19 shows the SEM picture of the spall plane for shot Rec05 with a tensile pulse of duration 250 ns. The SEM picture reveals a relatively rough fracture surface. At the higher magnifications, several micro-cracks and surface pits can be observed in the microstructure. These pits are probably formed when inter-grain boundary undergoes extensive damage, and the grains literally pop out of the microstructure. Moreover, the fracture/damage mode is observed to be predominantly brittle in nature.

3. Discussion and summary of results

In the present study, plate-impact experiments are conducted to obtain the stress threshold for inelasticity in Westerly granite by estimating its Hugoniot Elastic Limit (HEL) under shock-induced compression. These experiments are designed to also provide information on the spall strength following the shock-induced compression in the granite samples. The HEL for Westerly granite is estimated to be between 3.2 and 3.5 GPa. The spall strength is measured to be small ($\sim$50 MPa) with a shock pulse of duration 3 μs, and is found to be nearly independent of the applied compression level in the impact stress range of 0.7–5.0 GPa.

The post-impact samples show a well-defined spall plane with no apparent fragmentation at a shock compression level of 0.7 GPa. At higher impact stresses, fragmentation is observed up to 1.2 GPa, while the rock samples are reduced to essentially a powder at impact stress levels of above 1.8 GPa.

Furthermore, in the present study, soft recovery plate-impact experiments are conducted to better understand the threshold for initiation of micro-cracking in Westerly granite. These recovery experiments are conducted at the same stress level as the normal plate impact experiments ($\sim$0.7 GPa), and the duration of the tensile pulse is varied from 20 to 500 ns by varying the pre-set gap between the specimen and the momentum trap. Fig. 20 shows the spall strength vs. the time duration of the tensile pulse for all normal plate-impact and the soft-recovery plate-impact experiments conducted on Westerly granite. The results indicate that the stress pulse duration threshold for the initiation of spall is about 120 ns when the applied tensile stress level is $\sim$0.7 GPa. Moreover, it can be seen that tensile fracture in Westerly granite is a time-dependent phenomena, in which the spall strength depends on the duration of the tensile stress pulse. A general spall criterion along these lines was proposed by Tuler and Butcher [21]. They showed that the dynamic fracture (spall) phenomena is time-dependent, and that the critical spall stress level depends on the tensile stress pulse duration as $(\sigma-\sigma_0)^{\lambda}\Delta t = K$, where, σ is the applied tensile stress level, σ_0 is the stress below which spall will not occur even for very long stress pulse durations,
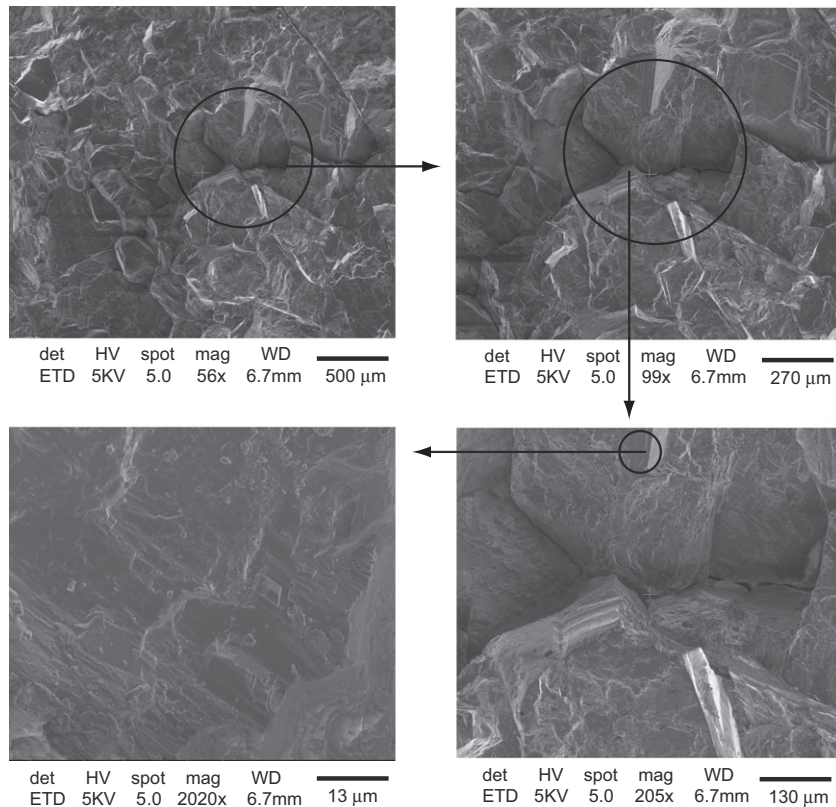
Fig. 19. Scanning electron microscopy of the spall plane for Shot Rec05 (tensile pulse duration of 250 ns).
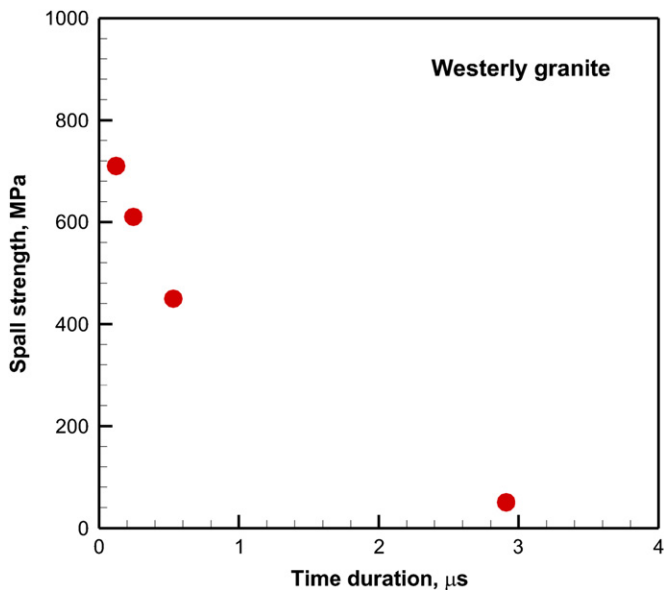

Fig. 20. Spall strength versus duration of the tensile pulse relationship in Westerly granite.

Δt is the duration of the applied tensile pulse, and λ and K are the material constants.

Detailed micro-structural analysis of the post-tested soft recovered specimen is conducted to understand the relationship between the extent of damage and the tensile stress pulse duration. For soft recovery experiments which do not show a clear spall signal (i.e., Shots Rec02 and Rec03), the recovered granite specimens show relatively large micro-cracks (30–40 μm in width) near the plane where the unloading waves from the flyer and target free surfaces intersect. Experiments, in which a clear spall signal is observed (i.e., Rec04, Rec05 and Rec06), the post-impacted granite specimens have a smaller thickness, indicating the creation of a distinct spall plane during the test. The spall plane reveals a relatively rough and a tortuous fracture surface. At higher magnification, several cracks and holes are detected on the spall plane. The fracture/damage mode is seen to be predominantly brittle in nature with damage initiating at the weak grain boundaries.

The experimental results presented here could be particularly useful for understanding damage threshold in geological materials under stress wave loading conditions. They also provide a rich set of experimental data for modeling inelasticity and code and/or model verification for rocks under well characterized loading conditions.

Acknowledgments

References

[1] Okeefe JD, Ahrens TJ. High-speed ejecta from a meteorite impact and planetary accretion. Eos Trans Am Geophys Union 1976;57274 1976;57.

[2] Ahrens TJ, Rubin AM. Impact-induced tensional failure in rock. J Geophys Res Planets 1993;98:1185–203.

[3] Millett JCF, Tsembelis K, Bourne NK. Longitudinal and lateral stress measurements in shock-loaded gabbro and granite. J Appl Phys 2000;87:3678–82.

[4] Melosh HJ. Shock viscosity and rise time of explosion waves in geologic media. J Appl Phys 2003;94:4320–5.

[5] Ai HA, Ahrens TJ. Simulation of dynamic response of granite: a numerical approach of shock-induced damage beneath impact craters. Int J Imp Eng 2006;33:1–10.

[6] Ai HA, Ahrens TJ. Effects of shock-induced cracks on the ultrasonic velocity and attenuation in granite. J Geophys Res Solid Earth 2007:112.

[7] Chen DP, He HL, Jing FQ. Delayed failure of the shock compressed inhomogeneous brittle material. J Appl Phys 2007:102.

[8] Willmott GR, Proud WG. The shock Hugoniot of Tuffisitic Kimberlite Breccia. Int J Rock Mech Min Sci 2007;44:228–37.

[9] Tilert D, Svedbjork G, Ouchterlony F, Nilsson B, Temun A, Mattsson L. Measurement of explosively induced movement and spalling of granite model blocks. Int J Impact Eng 2007;34:1936–52.

[10] Kovalev AE, Pavlovskii MN, Bel'skii VM, Komissarov VV. Elastoplastic behavior of marble, granite, and quartzite under shock compression. Tech Phys 2001;46: 686–9.

[11] Grady DE, Hollenbach RE. Dynamic fracture strength of rock. Geophys Res Lett 1979;6:73–6.

[12] Cohn SN, Ahrens TJ. Dynamic tensile strength of Lunar rock types. J Geophys Res 1981;86:1794–802.

[13] Barker LM, Hollenbach RE. Laser interferometer for measuring high velocities of any reflecting surface. J Appl Phys 1972;43:4669–75.

[14] Kumar P, Clifton RJ. Optical alignment of impact faces for plate impact experiments. J Appl Phys 1977;48:1366–7.

[15] Yuan F, Prakash V, Lewandowski JJ. Spall strength and Hugoniot elastic limit of a Zirconium-based bulk metallic glass under planar shock compression. J Maters Res 2007;22:402–11.

[16] Shazly M, Prakash V. Shock response of a gamma titanium aluminide alloy. J Appl Phys 2008;104:083513.

[17] Tsai L, Yuan F, Prakash V, Dandekar DP. Shock compression behavior of a S2-glass fiber reinforced polymer composite. J Appl Phys 2009;105:093526.

[18] Raiser G, Clifton RJ, Ortiz M. A soft-recovery plate impact experiment for studying microcracking in ceramics. Mech Maters 1990;10:43–58.

[19] Kumar P, Clifton RJ. A star-shaped flyer fpr plate-impact recovery experiments. J Appl Phys 1977;48:4850.

[20] Espinosa HD, Raiser G, Clifton RJ, Ortiz M. Performance of the star-shaped flyer in the study of brittle materials: three dimensional computer simulations and experimental observations. J Appl Phys 1992;72:3451–7.

[21] Tuler FR, Butcher BM. A criterion for the time dependence of dynamic fracture. Int J Fract 1968;4:431–7.